

1 **Importance of correlation effects in hcp iron revealed by a pressure-induced**  
2 **electronic topological transition**

3  
4  
5 K. Glazyrin<sup>1,2</sup>, L.V. Pourovskii<sup>3,4</sup>, L. Dubrovinsky<sup>1</sup>, O. Narygina<sup>5</sup>, C. McCammon<sup>1</sup>,  
6 B. Hewener<sup>6</sup>, V. Schünemann<sup>6</sup>, J. Wolny<sup>6</sup>, K. Muffler<sup>6</sup>, A. I. Chumakov<sup>7</sup>, W. Crichton<sup>7</sup>,  
7 M. Hanfland<sup>7</sup>, V. Prakapenka<sup>8</sup>, F. Tasnádi<sup>9</sup>, M. Ekholm<sup>3</sup>, , M. Aichhorn<sup>10</sup>, V. Vildosola<sup>11</sup>,  
8 A. V. Ruban<sup>12</sup>, M. I. Katsnelson<sup>13</sup>, I. A. Abrikosov<sup>9</sup>

9  
10 <sup>1</sup>*Bayerisches Geoinstitut, Universität Bayreuth, 95440 Bayreuth, Germany,*

11 <sup>2</sup>*Yale University, 06511 New Haven, CT, USA*

12 <sup>3</sup>*Swedish e-science Research Center (SeRC), Department of Physics, Chemistry and Biology (IFM),*  
13 *Linköping University, Linköping, Sweden*

14 <sup>4</sup>*Center de Physique Theorique, Ecole Polytechnique, 91128 Palaiseau Cedex, France*

15 <sup>5</sup>*School of Physics and Astronomy, University of Edinburgh, Edinburgh, UK*

16 <sup>6</sup>*Technische Universität Kaiserslautern, Kaiserslautern, Germany*

17 <sup>7</sup>*ESRF, F-38043 Grenoble Cedex, France*

18 <sup>8</sup>*GeoSoilEnviroCARS, University of Chicago, Argonne National Laboratory, Argonne, IL 60439, USA*

19 <sup>9</sup>*Department of Physics, Chemistry and Biology (IFM), Linköping University, Linköping, Sweden*

20 <sup>10</sup>*Institute of theoretical and computational physics, TU Graz, 8010 Graz, Austria*

21 <sup>11</sup>*Centro Atómico Constituyentes, GlyANN, CNEA, San Martin, Buenos Aires, Comisión Nacional de*  
22 *Investigaciones Científicas y Técnicas, Ciudad de Buenos Aires, Argentina*

23 <sup>12</sup>*Department of Materials Science and Engineering, Royal Institute of Technology, SE-10044, Stockholm,*  
24 *Sweden*

25 <sup>13</sup>*Radboud University Nijmegen, Institute for Molecules and Materials, 6525 AJ, Nijmegen, Netherlands*

26  
27  
28  
29  
30  
31  
32  
33  
34

35 **Abstract**

36 We discover that *hcp* phases of Fe and Fe<sub>0.9</sub>Ni<sub>0.1</sub> undergo an electronic topological  
37 transition at pressures of about 40 GPa. This topological change of the Fermi surface  
38 manifests itself through anomalous behavior of the Debye sound velocity, *c/a* lattice  
39 parameter ratio and Mössbauer center shift observed in our experiments. First-principles  
40 simulations within the dynamic mean field approach demonstrate that the transition is  
41 induced by many-electron effects. It is absent in one-electron calculations and represents  
42 a clear signature of correlation effects in *hcp* Fe.

43  
44  
45  
46

47 Iron is the most abundant element on our planet. It is one of the most important  
48 technological materials and, at the same time, one of the most challenging elements for  
49 the modern theory. As a consequence, the study of iron and iron-based alloys has been a  
50 focus of experimental and computational research over the past decades. Recently,  
51 investigations of phase relations and physical properties of iron and its alloys at high  
52 pressure led to new exciting discoveries including evidence for a body-centred-cubic  
53 (bcc) phase of iron-nickel alloy at conditions of the Earth's core [1] and the observation  
54 of superconductivity in the high-pressure hexagonal close packed (*hcp*) phase of iron in  
55 the pressure range 15-30 GPa and at temperatures below 2 K [2].

56 While the structural properties of iron and iron-nickel alloys at pressures below 100  
57 GPa are well established [3], their electronic and magnetic properties are still debated.  
58 The  $\alpha$ -phases (*bcc*) of Fe and Fe<sub>0.9</sub>Ni<sub>0.1</sub> are ferromagnetic at ambient conditions, but an  
59 accurate description of the electronic structure of  $\alpha$ -Fe and its high-temperature  
60 magnetism require a proper treatment of the many-electron effects [4]. The  $\gamma$ -phases  
61 (face-centered cubic, *fcc*) are believed to have complex incommensurate magnetic ground  
62 states, which are still not reproduced by theory [5]. The importance of correlation effects  
63 for the description of the  $\alpha$ - to  $\gamma$ -phase transition in Fe at elevated temperature and  
64 ambient pressure has been recently underlined [6]. The  $\epsilon$ -phases (*hcp*) of Fe and  
65 Fe<sub>0.9</sub>Ni<sub>0.1</sub> were previously believed to be nonmagnetic [7]; however recent theoretical  
66 work showed that a collinear antiferromagnetic state (AFM-II) [8–10] or a more complex

67 AFM state [11] have lower energy than the nonmagnetic state. Nevertheless, the AFM-II  
68 phase could not be resolved in Mössbauer experiments. Moreover, theoretical estimates  
69 of the Néel temperature  $T_N$  yield a maximum value of  $\sim 69$  K for *hcp* Fe at the transition  
70 pressure (12 GPa), followed by a decrease with increasing pressure [12]. Although nickel  
71 atoms are predicted to enhance the magnetic moments on neighboring iron atoms, there is  
72 no evidence that  $\epsilon$ -Fe<sub>0.9</sub>Ni<sub>0.1</sub> is a static antiferromagnet down to at least 11 K at  
73 21 GPa [10], implying that direct comparison is unreliable between static (0 K) *ab initio*  
74 calculations for AFM  $\epsilon$ -Fe and room temperature experimental data that clearly indicate a  
75 paramagnetic phase. It is worth noting that *hcp* Fe becomes superconducting in the same  
76 pressure range [2], and that the mechanism of superconductivity is believed to be  
77 unconventional [13]. These observations indicate that the physical behavior of *hcp* Fe at  
78 moderate pressures below 70 GPa is complex and the role of correlation effects beyond  
79 the standard density-functional (DFT) approach in the physics of this material is not well  
80 understood.

81 In order to unravel the evolution of the electronic structure in *hcp* Fe and Fe<sub>0.9</sub>Ni<sub>0.1</sub>  
82 under pressure we have carried out a combined experimental and theoretical  
83 investigation. We have extracted the Debye sound velocity  $V_D$  for pure Fe and Fe<sub>0.9</sub>Ni<sub>0.1</sub>  
84 alloy from nuclear inelastic scattering (NIS) experiments as well as precisely measured  
85 the lattice parameter  $c/a$  ratio and the Mössbauer centre shift in the pressure range from  
86 12 to 70 GPa. All of our results show anomalous behavior at a similar pressure  $\sim 40$  GPa.  
87 Our state-of-the-art *ab initio* simulations within the dynamical mean-field theory [14–16]  
88 reveal an electronic topological transition (ETT) in the *hcp* phase of iron at pressures of  
89 about 30-40 GPa, providing an explanation of the experimentally observed anomalies.  
90 The absence of the ETT in conventional one-electron DFT calculations demonstrates that  
91 many-body correlation effects determine the Fermi surface topology of paramagnetic *hcp*  
92 Fe, and, therefore, essential for the correct description of the complex physical  
93 phenomena observed in this material.

94 Figure 1 summarizes our experimental measurements of the Debye sound velocity  $V_D$   
95 for Fe and Fe<sub>0.9</sub>Ni<sub>0.1</sub> extracted from NIS experiments (technical details are given in  
96 Supplementary Information [17]). The experimental data show a softening of  $V_D$  in the  
97 pressure range 42-52 GPa. To verify our results we also analyzed the available

98 literature [18–21] and conclude that the same softening of  $V_D$  has been observed at  
99 pressures of 40-50 GPa. The phenomenon was not given much attention in the previous  
100 publications, perhaps due to data scatter and the uncertainties of individual data points.

101 The softening of the Debye sound velocity in Fig. 1 is weak, so we made further  
102 investigations. We measured the lattice parameters of *hcp*-Fe in a diamond anvil cell  
103 (DAC) on compression to ~65 GPa in quasi-hydrostatic He pressure transmitting medium  
104 at ambient temperature and found an anomaly in  $c/a$  at about 40 GPa (Fig. 2a), consistent  
105 with the pressure at which  $V_D$  shows softening. The pressure dependence of the  $c/a$  ratio  
106 in *hcp* Fe has been the subject of several previous experimental studies [22–27] that were  
107 mainly focused on much higher pressures. However, a closer inspection of the results by  
108 Dewaele *et al.* [24] shows very good agreement with our data (*Fig. S.1.3* [17]). Also, an  
109 anomalous behavior of  $c/a$  was reported at about 50 GPa based on a limited number of  
110 data points collected in DAC experiments using a non-hydrostatic (NaCl) pressure-  
111 transmitting medium [27].

112 Mössbauer spectroscopy can also be a powerful method to detect pressure-induced  
113 transitions [28]. We performed Mössbauer experiments on pure Fe and  $\text{Fe}_{0.9}\text{Ni}_{0.1}$  up to  
114 60 GPa in a DAC loaded with He as a quasi-hydrostatic pressure transmitting medium,  
115 and observed a large anomaly in the center shift variation with pressure at 40-45 GPa  
116 (Fig. 2b). Our theoretical calculations demonstrate that the anomaly cannot be explained  
117 by changes of the electron density at the nuclei and, correspondingly, of the isomer  
118 shift [17]. Therefore, the anomaly must be associated with the second-order Doppler  
119 shift [28].

120 We have shown from three independent experimental methods pressure-induced  
121 anomalies in the pressure range 40-50 GPa. We note that X-ray diffraction does not  
122 reveal any crystallographic structural change of *hcp*-Fe and  $\text{Fe}_{0.9}\text{Ni}_{0.1}$  at the same  
123 conditions [1,29,30], and as discussed above, there is no long range magnetic order in the  
124 *hcp* phase of Fe detected by experiments. The observed anomalies must therefore be  
125 associated with changes in the electronic state of paramagnetic *hcp*-Fe and  $\text{Fe}_{0.9}\text{Ni}_{0.1}$ . To  
126 address this question we made a theoretical investigation of the electronic structure of  $\epsilon$ -  
127 Fe at moderate pressures in the range 12-70 GPa. We employed a state-of-the-art fully  
128 self-consistent technique [16] combining full-potential linearized augmented plain-wave

129 (LAPW) band structure method with the dynamical mean-field theory (DMFT) treatment  
 130 of the on-site Coulomb repulsion between Fe  $3d$  states [17]. The DMFT quantum  
 131 impurity problem was solved using the exact Continuous-time strong-coupling Quantum  
 132 Monte-Carlo method [31]. A combination of LDA and DMFT has been applied  
 133 previously to investigate thermodynamic stability [6] and to describe the magnetic  
 134 properties [4] of paramagnetic  $bcc$  Fe at ambient pressure, which justifies the choice of  
 135 method for this work.

136 The LDA+DMFT Fermi surfaces and  $\mathbf{k}$ -resolved spectral functions for two different  
 137 volumes are shown in Fig. 3. The  $hcp$  phase of Fe is predicted to be weakly correlated,  
 138 with the average mass enhancement decreasing from 1.43 at 16 GPa to 1.25 at 69 GPa,  
 139 indicating a reduced correlation strength at smaller volumes. Sharp bands in the vicinity  
 140 of the Fermi level  $\varepsilon_F$  and a noticeable shift of bands toward  $\varepsilon_F$  compared to the LDA  
 141 picture (Fig. 3 (e) and (f)) are the usual features of a Fermi liquid. Most interestingly, the  
 142 hole-like bands at the  $\Gamma$  and  $\mathbf{L}$  points visible at smaller volume are found *below*  $\varepsilon_F$  at  
 143  $V=10.4 \text{ \AA}^3/\text{at}$ . Hence, the DMFT calculations show that the topology of the Fermi surface  
 144 changes under compression. Indeed a comparison of Figs. 3 (a) and (b) shows that hole  
 145 pockets appears at  $\Gamma$  and  $\mathbf{L}$  with decreasing volume, and therefore  $hcp$  Fe undergoes an  
 146 *electronic topological transition* [32] under applied pressure. The actual ETT takes place  
 147 at  $P \sim 30$  GPa. It is remarkable that the observed ETT is absent in the LDA calculations; it  
 148 appears only upon inclusion of correlation effects.

149 The effects of ETT on the lattice properties of metals within the one-electron  
 150 approximation are well understood [33]. The elastic moduli  $C_{ii}$  calculated at the  
 151 condition of constant particle number at the deformation contains the contribution

$$152 \quad \delta C_{ii} = -\frac{1}{V_0} \sum_{\lambda} \left( \frac{\partial \zeta_{\lambda}}{\partial u_i} \right)^2 \delta(\zeta_{\lambda}), \quad (1)$$

153 where  $\zeta_{\lambda} = \varepsilon_{\lambda} - \varepsilon_F$ , and  $\varepsilon_{\lambda}$  denotes the single-particle energies.  $\zeta_{\lambda}$  is singular near the  
 154 ETT, and this singular contribution has the same singularity as  $-N(\varepsilon_F)$ . This means, in  
 155 particular, that the peculiarity in the Debye sound velocity is  $\Delta V_D \sim -\delta N(E_F)$ , where  $\delta N(E_F)$   
 156 is the change in the density of states (DOS) at the Fermi level due to ETT. In the case of  
 157 an appearance of a new hole pocket below the critical volume  $V_{\text{ETT}}$  the change in DOS is

158  $\delta N(E_F) \sim (V_{ETT} - V)^{1/2}$ , hence the one-electron theory predicts the existence of square-root-  
 159 down-shaped peculiarity at the ETT. Our DMFT calculations show that in the case of  
 160 *hcp*-Fe at moderate compression one should use the Fermi-liquid theory of ETT [34]. In  
 161 this case many-electron effects cause the singularity of the thermodynamic potential  $\Omega$  at  
 162 ETT to be two-sided. Still the leading term is a square root in  $\Delta V_D$  on one side of the  
 163 transition, while the peculiarity on the other side of the transition is one power weaker.

164 The Debye temperature  $\theta_D$  also has a singularity as  $-N(\varepsilon_F)$ , and lattice heat capacity  
 165 at low temperature  $T \ll \theta_D$  has the same singularity as the electron heat capacity. The  
 166 thermal expansion coefficient proportional to the derivative of  $\theta_D$  with respect to  
 167 deformation has a stronger singularity at these temperatures, like  $\frac{\partial N(\varepsilon_F)}{\partial \varepsilon_F}$ , that is  
 168 divergent at the point of ETT (e.g., [35]). It is important to stress, however, that the  
 169 Debye model is qualitatively incorrect in the situation of ETT. Strong anomalies of the  
 170 phonon spectra in the harmonic approximation occur in a relatively small part of the  
 171 Brillouin zone near the  $\Gamma$  point and the average phonon frequency over the whole  
 172 Brillouin zone, which is relevant for thermodynamics at  $T \approx \theta_D$ , is weaker by a factor of  
 173  $\varepsilon_F - \varepsilon_c$ , where  $\varepsilon_c$  is the Van Hove singularity energy [36]. However, if we take into  
 174 account quasiharmonic and anharmonic effects, i.e., the temperature dependence of  
 175 phonon frequencies due to thermal expansion and phonon-phonon interactions, the  
 176 singularities again enhance and become like  $N(\varepsilon_F)$  in average phonon frequencies and  
 177 like  $\frac{\partial N(\varepsilon_F)}{\partial \varepsilon_F}$  in the elastic moduli [36].

178 For *hcp* metals ETTs have been associated with anomalies in the lattice parameter  
 179 ratio  $c/a$  in the vicinity of the transition [37–40]. The dependence of lattice constants on  
 180 the external parameters is less singular than  $C_{ii}$  since they are related to the first  
 181 derivatives of the thermodynamic potential, while  $C_{ii}$  are related to the second  
 182 derivatives. This means that the anomaly in the  $c/a$  ratio at zero temperature should be  
 183 hardly visible but at finite (and sufficiently high) temperatures it is proportional to  $N(\varepsilon_F)$   
 184 via the anomaly of the thermal expansion coefficient, discussed above. The same is true  
 185 for the second-order Doppler shifts of the Mössbauer spectra related to the heat capacity

186 and, thus, with the average phonon frequencies over the Brillouin zone. Thus, the theory  
187 of ETT provides a convincing explanation of the experimentally observed anomalies of  
188 the sound velocity,  $c/a$  ratio and center shift at 40-45 GPa.

189 To conclude, we observe the electronic isostructural transition of *hcp* Fe and  $\text{Fe}_{0.9}\text{Ni}_{0.1}$   
190 at a pressure of  $\sim 40$  GPa. The presence of the transition is confirmed by three  
191 independent experimental approaches – nuclear inelastic scattering,  $c/a$  ratio  
192 measurement, and Mössbauer center shift determination. The theoretical calculations  
193 carried out by means of state-of-the-art *ab initio* methods explain the anomalies in terms  
194 of a change of the Fermi surface topology, a so-called electronic topological transition.  
195 The existence of the ETT in many-body calculations and its absence in one-electron  
196 calculations is a clear signature of correlation effects in the paramagnetic phase of *hcp*  
197 Fe. Therefore, advanced approaches beyond the density functional theory are needed to  
198 understand the complex physics of this material. Our results also point out to possible  
199 importance of many-body effects in other itinerant metallic systems at high-pressure  
200 conditions.

201 We are grateful to Prof. A. Georges for useful discussion. The funding provided  
202 by Swedish e-science Research Centre (SeRC), the Swedish Research Council via grant  
203 621-2011-4426, and the Swedish Foundation for Strategic Research (SSF) programs SRL  
204 grant 10-0026 and “Multifilms”, as well as financial support from German Science  
205 Foundation (DFG) and German Ministry for Education and Research (BMBF) are  
206 acknowledged. Calculations have been performed at the Swedish National Infrastructure  
207 for Computing (SNIC). We acknowledge the European Synchrotron Radiation Facility  
208 for provision of synchrotron radiation facilities on beamlines ID09a and ID18.

209

## 210 REFERENCES

- 211 [1] L. Dubrovinsky, N. Dubrovinskaia, O. Narygina, I. Kantor, A. Kuznetsov, V. B.  
212 Prakapenka, L. Vitos, B. Johansson, A. S. Mikhaylushkin, S. I. Simak, and I. A.  
213 Abrikosov, *Science* **316**, 1880 (2007).
- 214 [2] K. Shimizu, T. Kimura, S. Furomoto, K. Takeda, K. Kontani, Y. Onuki, and K.  
215 Amaya, *Nature* **412**, 316 (2001).
- 216 [3] R. Boehler, *Rev. Geophys.* **38**, 221 (2000).

217 [4] A. I. Lichtenstein, M. I. Katsnelson, and G. Kotliar, Phys. Rev. Lett. **87**, 067205  
218 (2001).

219 [5] I. A. Abrikosov, A. E. Kissavos, F. Liot, B. Alling, S. I. Simak, O. Peil, and A.  
220 V. Ruban, Phys. Rev. B **76**, 014434 (2007).

221 [6] I. Leonov, A. Poteryaev, V. Anisimov, and D. Vollhardt, Phys. Rev. Lett. **106**,  
222 106405 (2011).

223 [7] G. Cort, R. D. Taylor, and J. O. Willis, J. Appl. Phys. **53**, 2064 (1982).

224 [8] G. Steinle-Neumann, L. Stixrude, and R. E. Cohen, Phys. Rev. B **60**, 791 (1999).

225 [9] G. Steinle-Neumann, R. E. Cohen, and L. Stixrude, J. Phys.: Condens. Matter **16**,  
226 S1109 (2004).

227 [10] A. B. Papandrew, M. S. Lucas, R. Stevens, I. Halevy, B. Fultz, M. Y. Hu, P.  
228 Chow, R. E. Cohen, and M. Somayazulu, Phys. Rev. Lett. **97**, 087202 (2006).

229 [11] R. Lizárraga, L. Nordström, O. Eriksson, and J. Wills, Phys. Rev. B **78**, 064410  
230 (2008).

231 [12] V. Thakor, J. B. Staunton, J. Poulter, S. Ostanin, B. Ginatempo, and E. Bruno,  
232 Phys. Rev. B **67**, 180405 (2003).

233 [13] I. I. Mazin, D. A. Papaconstantopoulos, and M. J. Mehl, Phys. Rev. B **65**, 100511  
234 (2002).

235 [14] A. Georges, G. Kotliar, W. Krauth, and M. J. Rozenberg, Rev. Mod. Phys. **68**, 13  
236 (1996).

237 [15] G. Kotliar, S. Y. Savrasov, K. Haule, V. S. Oudovenko, O. Parcollet, and C. A.  
238 Marianetti, Rev. Mod. Phys. **78**, 865 (2006).

239 [16] M. Aichhorn, L. Pourovskii, V. Vildosola, M. Ferrero, O. Parcollet, T. Miyake,  
240 A. Georges, and S. Biermann, Phys. Rev. B **80**, 085101 (2009).

241 [17] see Supplementary information at [URL] for details of experiments and  
242 theoretical simulations.

243 [18] H. K. Mao, J. Xu, V. V. Struzhkin, J. Shu, R. J. Hemley, W. Sturhahn, M. Y. Hu,  
244 E. E. Alp, L. Vocadlo, D. Alfè, G. D. Price, M. J. Gillan, M. Schwoerer-Böhning, D.  
245 Häusermann, P. Eng, G. Shen, H. Giefers, R. Lübbers, and G. Wortmann, Science **292**,  
246 914 (2001).

247 [19] R. Lübbers, H. F. Grünsteudel, A. I. Chumakov, and G. Wortmann, Science **287**,



248 1250 (2000).

249 [20] J. C. Crowhurst, A. F. Goncharov, and J. M. Zaug, in *Advances in High-Pressure*  
250 *Technology for Geophysical Applications* (Elsevier, 2005), pp. 3–23.

251 [21] J. F. Lin, V. V. Struzhkin, W. Sturhahn, E. Huang, J. Zhao, Y. M. Hu, E. E. Alp,  
252 H.-K. Mao, N. Boctor, and R. J. Hemley, *Geophys. Res. Lett.* **30**, (2003).

253 [22] H.-K. Mao, Y. Wu, L. C. Chen, J. F. Shu, and A. P. Jephcoat, *J. Geophys. Res.*  
254 **95**, 21737 (1990).

255 [23] L. S. Dubrovinsky, S. K. Saxena, F. Tutti, S. Rekhi, and T. LeBehan, *Phys. Rev.*  
256 *Lett.* **84**, 1720 (2000).

257 [24] A. Dewaele, P. Loubeyre, F. Occelli, M. Mezouar, P. I. Dorogokupets, and M.  
258 Torrent, *Phys. Rev. Lett.* **97**, 215504 (2006).

259 [25] Y. Ma, M. Somayazulu, G. Shen, H. Mao, J. Shu, and R. J. Hemley, *Physics of*  
260 *the Earth and Planetary Interiors* **143–144**, 455 (2004).

261 [26] R. Boehler, D. Santamaría-Pérez, D. Errandonea, and M. Mezouar, *Journal of*  
262 *Physics: Conference Series* **121**, 022018 (2008).

263 [27] S. Ono, T. Kikegawa, N. Hirao, and K. Mibe, *American Mineralogist* **95**, 880  
264 (2010).

265 [28] W. Potzel, M. Steiner, H. Karzel, W. Schiessl, M. Köfferlein, G. M. Kalvius, and  
266 P. Blaha, *Phys. Rev. Lett.* **74**, 1139 (1995).

267 [29] C. S. Yoo, J. Akella, A. J. Campbell, H. K. Mao, and R. J. Hemley, *Science* **270**,  
268 1473 (1995).

269 [30] W. L. Mao, A. J. Campbell, D. L. Heinz, and G. Shen, *Physics of the Earth and*  
270 *Planetary Interiors* **155**, 146 (2006).

271 [31] P. Werner, A. Comanac, L. de’ Medici, M. Troyer, and A. Millis, *Phys. Rev.*  
272 *Lett.* **97**, 076405 (2006).

273 [32] I. M. Lifshitz, *Soviet Phys. JETP* **11**, 1130 (1960).

274 [33] M. I. Katsnelson, I. I. Naumov, and A. V. Trefilov, *Gpht* **49**, 143 (1994).

275 [34] M. I. Katsnelson and A. V. Trefilov, *Phys. Rev. B* **61**, 1643 (2000).

276 [35] P. Souvatzis, O. Eriksson, and M. I. Katsnelson, *Phys. Rev. Lett.* **99**, 015901  
277 (2007).

278 [36] V. G. Vaks and A. V. Trefilov, *J. Phys.: Condens. Matter* **3**, 1389 (1991).

- 279 [37] S. Meenakshi, V. Vijayakumar, B. K. Godwal, and S. K. Sikka, Phys. Rev. B **46**,  
280 14359 (1992).
- 281 [38] D. L. Novikov, A. J. Freeman, N. E. Christensen, A. Svane, and C. O. Rodriguez,  
282 Phys. Rev. B **56**, 7206 (1997).
- 283 [39] V. V. Kechin, Phys. Rev. B **63**, 045119 (2001).
- 284 [40] Z. Li and J. S. Tse, Phys. Rev. Lett. **85**, 5130 (2000).
- 285

286 **Figure captions:**

287 **Figure 1 (color online)**

288 Debye sound velocity  $V_D$  as a function of pressure for pure iron (filled black squares, -1-) and  $\text{Fe}_{0.9}\text{Ni}_{0.1}$  alloy (open triangles, -2-). The upper axis shows the density scale. Also shown are literature data on sound velocities obtained with NIS (open circles [18], -4- and half-filled circles [19], -5-), and impulsive stimulated light scattering (ISLS) measurements [20] (circles with crosses, -6-) for pure  $\epsilon$ -Fe, as well as NIS data [21] for  $\epsilon$ - $\text{Fe}_{0.92}\text{Ni}_{0.08}$  (blue open squares, -3-). Experimental data presented in the figure show the softening of  $V_D$  in a pressure region of 42-52 GPa.

295

296 **Figure 2**

297 Experimental pressure dependence of (a) *hcp* phase lattice parameter *c/a* ratio and (b) the Mössbauer centre shift based on several experimental datasets for pure iron (red circles) and for  $\text{Fe}_{0.9}\text{Ni}_{0.1}$  alloy (blue circles). The centre shift values are given relative to pure *bcc* iron. Straight grey lines in (a) are guides for the eye.

301

302 **Figure 3.**

303 The LDA+DMFT  $\mathbf{k}$ -resolved spectral function  $A(\mathbf{k}, E)$  ( in  $V_{\text{at}}/\text{eV}$ , where  $V_{\text{at}}$  is the volume per atom) of *hcp* Fe at volumes of  $8.9 \text{ \AA}^3/\text{at}$  (a) and  $10.4 \text{ \AA}^3/\text{at}$  (b) corresponding to pressures of 69 and 15.4 GPa, respectively. The energy zero is taken at the Fermi level. The hole-like bands at the  $\Gamma$  and  $L$  points at volume  $8.9 \text{ \AA}^3/\text{at}$  (indicated by the white arrows) are *below*  $E_F$  at  $V=10.4 \text{ \AA}^3/\text{at}$ . The corresponding LDA band structures are shown in *e* and *d*, respectively. In (e) and (f) the corresponding LDA+DMFT Fermi surfaces are shown for the same volumes. The full Fermi surface is plotted on the left-hand side and its cut along the  $\Gamma$ -M direction is displayed in the right-hand side. Changes of the FS topology around the  $L$  and  $\Gamma$  points are clearly seen.

312

313

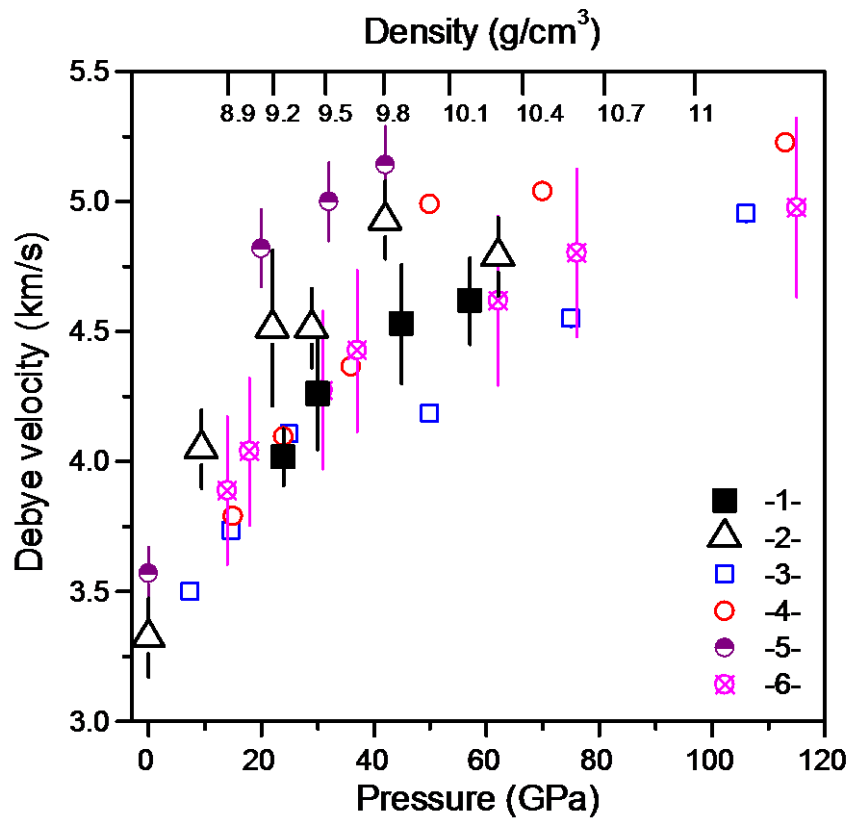
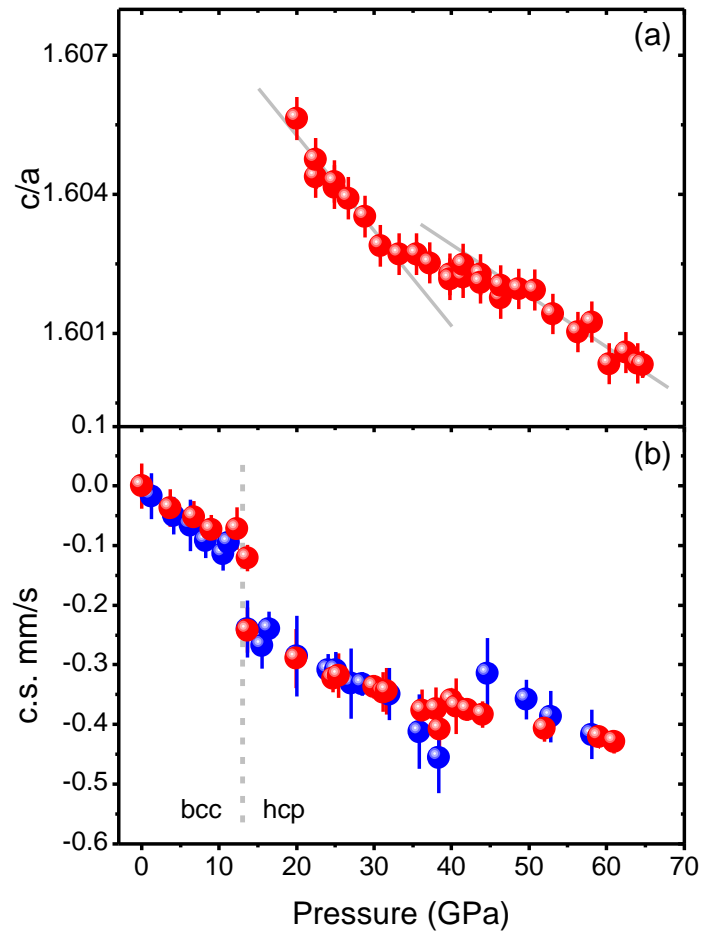
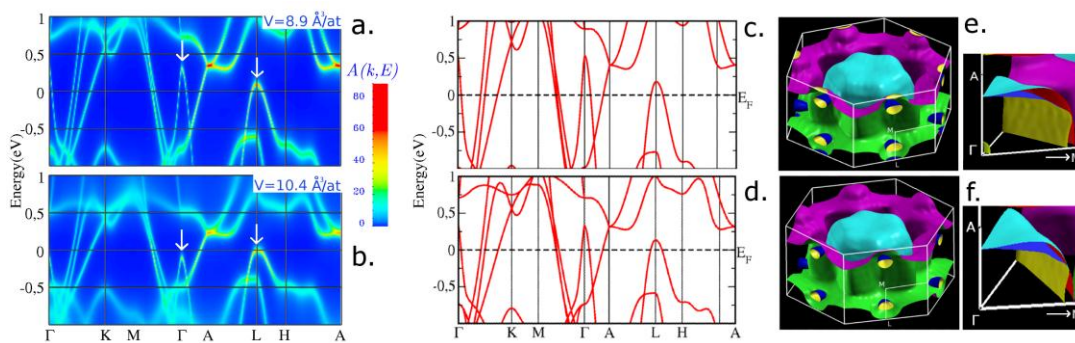


FIG. 1 (color online)



**FIG. 2**



**FIG. 3.**

315

316

317 SUPPLEMENTARY INFORMATION

318 *1. Experimental details*

319

320 For the preparation of the iron sample we used enriched  $^{57}\text{Fe}$  of 99.99% purity. The  
321  $\text{Fe}_{0.9}\text{Ni}_{0.1}$  samples were prepared by mixing appropriate amounts of  $^{57}\text{Fe}$  enriched iron  
322 and nickel powder of 99.999% purity. The mixture was compressed to 2 GPa in a piston-  
323 cylinder apparatus, heated above the melting point and subsequently quenched.

324 To achieve high pressures in different experiments we used two types of diamond  
325 anvil cells: one piston-cylinder conventional cell for Mossbauer experiments, with He gas  
326 for quasi-hydrostatic conditions loaded into a chamber of Re gasket, and for nuclear  
327 inelastic x-ray scattering (NIS) another panoramic cell produced in Bayerisches  
328 Geoinstitut. Special types of new cells slits make it possible to measure nuclear forward  
329 scattering (NFS) or X-Ray diffraction patterns at the same time as NIS, and, due to the  
330 specific geometry of NIS cells, Be was chosen as a material for the gaskets. We used LiF  
331 as a pressure medium for the NIS cells. In both experiments we used diamonds with  
332  $250\mu\text{m}$  culet size and small ruby chips to measure the pressure inside gasket chambers.  
333 The prepared gasket chambers were  $60\mu\text{m}\cdot 20\mu\text{m}$  and  $100\mu\text{m}\cdot 30\mu\text{m}$  (diameter·height) for  
334 NIS and Mossbauer experiments, respectively.

335 NIS studies were carried out at the beam line ID18 [S1] (ESRF, Grenoble); the  
336 details of the experiment are described in Lübbert et al. [S2] and references therein. Data  
337 analysis was performed using program DOS-2.1 according to the calculation procedure  
338 described in Kohn and Chumakov [S3], and more details of the calculation procedure is  
339 described in Sturhahn [S4] and references therein.

340 To extract the partial density of states for iron (PDOS) using NIS we employed the  
341 following procedure. First, we collected absorption spectra of the sample enriched with  
342  $^{57}\text{Fe}$  as a function of the energy of incident radiation (NIS spectra Fig S1.1). After  
343 extracting the elastic contribution to the NIS spectra, we used DOS-2.1 software to  
344 extract the PDOS. Next, we calculated Debye sound velocities ( $V_D$ ) using the  
345 relation [S5]:

346 
$$\rho \cdot V_D^3 = \frac{4 \cdot \pi \cdot \tilde{m}}{h^3} \cdot \lim_{E \rightarrow 0} \frac{E^2}{D(E)},$$

347 where  $\rho$  is the density of the material;  $m$  is the mass of the nuclear resonant isotope  
348 ( $^{57}\text{Fe}$ );  $h$  is Planck's constant;  $D(E)$  is the iron PDOS and  $E$  is energy.

349 We determined the equation of state for the *hcp* phase of Fe and  $\text{Fe}_{0.9}\text{Ni}_{0.1}$  (the  
350 variation of  $\rho$  with pressure) and the bulk modulus in a separate synchrotron X-ray  
351 diffraction experiment on beam lines ID09a (ESRF, Grenoble) and IDD-13 (APS,  
352 Argonne). The parameters derived from a fit to the Birch-Murnaghan equation of state for  
353 *hcp*- $\text{Fe}_{0.9}\text{Ni}_{0.1}$  are bulk modulus  $K=159(3)$  GPa,  $K'=4.78(9)$  and  $V_0=6.77(1)$   $\text{cm}^3/\text{mol}$ , and  
354 for *hcp*-Fe EOS these parameters have values indistinguishable from the values reported  
355 in previous studies [S6,S7]. We collected a set of X-ray diffraction data for pure Fe in a  
356 compression run up to  $\sim 65$  GPa (quasi-hydrostatic pressure medium - He). We used the  
357 ruby fluorescence method for pressure determination [S8] and Fullprof [S9] and  
358 Unitcell [S10] programs to extract the  $c$  and  $a$  lattice parameters for *hcp*-Fe. There is a  
359 remarkable agreement between values calculated by these programs. A representative X-  
360 diffraction pattern from the second run is shown in Fig. S1.2. The results of our runs are  
361 compared in Fig. S1.3 with data from the literature [S11,S12].

362  $^{57}\text{Fe}$  Mössbauer spectra (MS, Fig S1.4) were recorded at room temperature in  
363 transmission mode on a constant acceleration Mössbauer spectrometer using a nominal  
364 370 MBq  $^{57}\text{Co}$  high specific activity source in a 12  $\mu\text{m}$  Rh matrix (point source). The  
365 velocity scale was calibrated relative to 25  $\mu\text{m}$   $\alpha$ -Fe foil. Mössbauer spectra were fitted to  
366 Lorentzian lineshapes using the commercially available fitting program NORMOS  
367 written by R.A. Brand (distributed by Wissenschaftliche Elektronik GmbH, Germany).  
368 Collection time for each spectrum varied from 24 to 48 h.

369 In our experiments the *bcc*  $\alpha$ -phase transforms to the *hcp*  $\varepsilon$ -phase at 10-13 GPa, in  
370 good agreement with literature data [S13,S14]. The center shift in *hcp*-Fe and *hcp*-  
371  $\text{Fe}_{0.9}\text{Ni}_{0.1}$  gradually decreases with pressure, up to 40-45 GPa. In this pressure range we  
372 observe an abrupt increase of the center shift by  $\sim 0.15$  mm/s in  $\text{Fe}_{0.9}\text{Ni}_{0.1}$  and a smaller  
373 value of  $\sim 0.05$  mm/s in pure iron (Fig. 2, main text). Upon further compression to 60 GPa  
374 we see no sign of further irregular behavior. The discontinuity was observed in several  
375 independent DAC loadings. Previous X-ray diffraction measurements have not revealed  
376 any structural transformation in the pressure range 13-60 GPa in both *hcp* Fe and  
377  $\text{Fe}_{0.9}\text{Ni}_{0.1}$  [S15,S16].

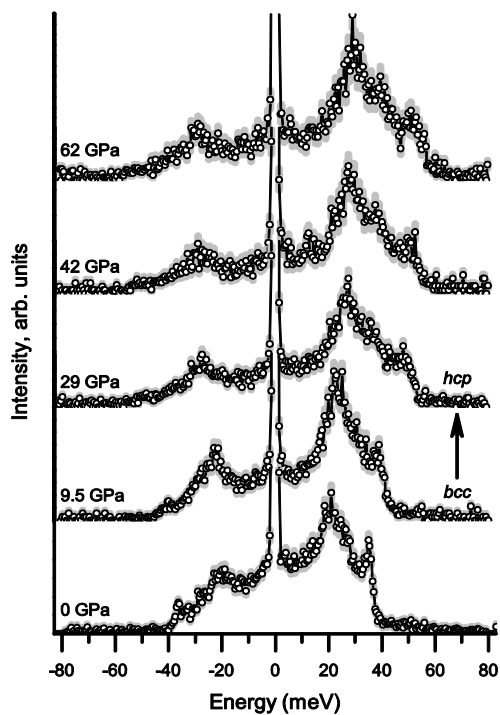


**Fig. S1.1** Nuclear inelastic scattering absorption spectra at various pressures measured on Fe<sub>0.9</sub>Ni<sub>0.1</sub>.

378

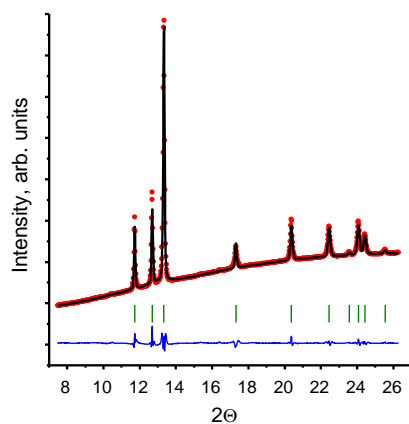


**Fig. S1.2** X-ray diffraction pattern of pure Fe obtained at 64.7(1) GPa. The red data points are the experimental data. The black line, the blue line and the green vertical lines represent a Le Bail fit of data (Fullprof), difference between the data and the model, and positions of *hcp*-Fe diffraction lines, respectively.



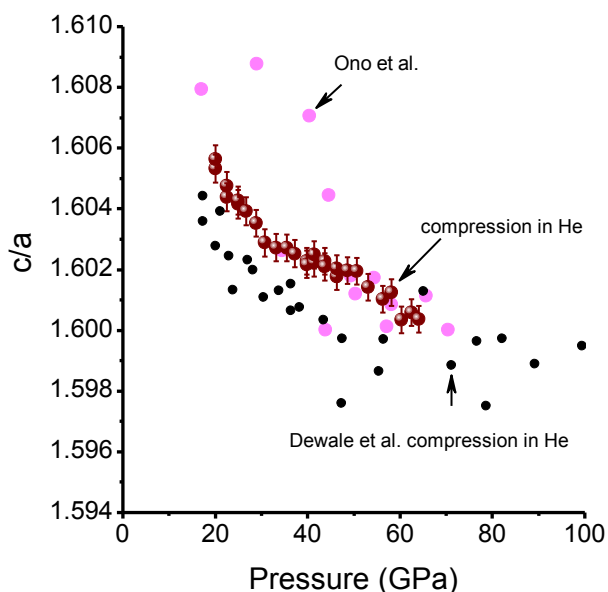


**Fig S1.3** Variation of  $c/a$  lattice parameter ratio as a function of pressure. Dark red points correspond to our data (He pressure medium), and pink points indicate those obtained by Ono et al. [S11] (NaCl pressure medium, experimental uncertainties unknown) collected during compression runs. The Dewaele *et al.* [S12] data are shown by black closed circles.

379

380

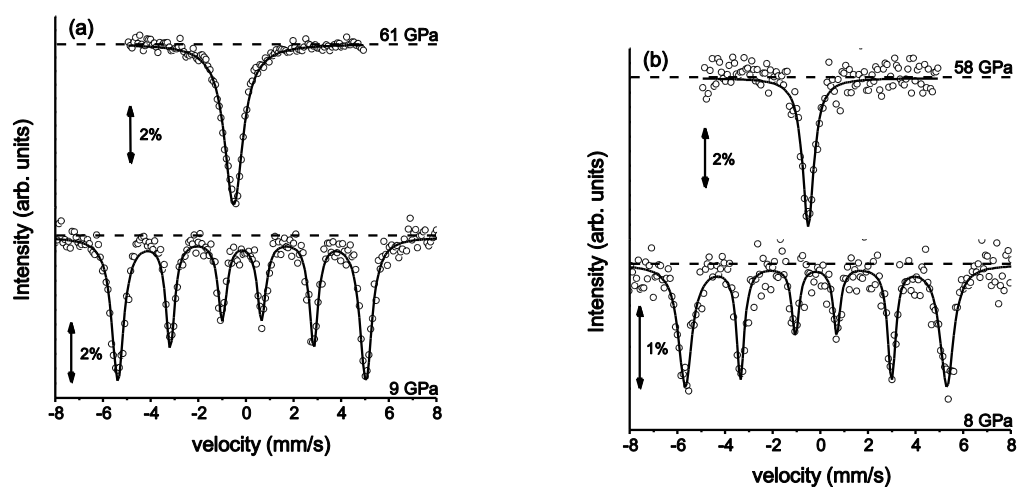


**Fig. S1.4** Representative Mössbauer spectra of (a) pure Fe and (b)  $\text{Fe}_{0.9}\text{Ni}_{0.1}$  samples at the indicated pressures. Solid lines represent model fits.

381 **2 Theoretical Simulations**

382 **2.1 Local-density approximation+dynamical mean-field theory (LDA+DMFT)**  
383 *approach*

384 Our LDA+DMFT calculations have been performed with a full-potential fully-self  
385 consistent implementation [S17,S18] combining the dynamical-mean-field-theory [S19–  
386 S21] and a highly precise full-potential linearized augmented plane wave (FLAPW)  
387 electronic structure technique [S22]. The DMFT quantum impurity problem was solved  
388 by the continuous-time quantum Monte Carlo (CTQMC) [S23] method. At the beginning  
389 of each LDA+DMFT iteration, the eigenvalues and eigenvectors of the Kohn-Sham  
390 problem were obtained by the FLAPW code. Wannier-like functions for the Fe-3*d* shell  
391 were then constructed by projecting local orbitals onto a set of FLAPW Bloch states  
392 located within the energy window from -9.5 to 9.2 eV (details of the projection procedure  
393 can be found elsewhere [S17]). We then introduced a local Coulomb interaction acting  
394 between those Wannier orbitals and solved the resulting many-body problem within the  
395 DMFT framework. After completing the DMFT cycle we calculated the resulting density  
396 matrix in the Bloch states' basis, which was then used to recalculate the charge density  
397 and update the Kohn-Sham potential at the next iteration [S18].

398 We have employed the density-density form of the local Coulomb interaction in the  
399 spherical approximation, in which case the interaction matrix is fully specified by the  
400 parameters  $U=3.4$  eV and  $J=0.9$  eV, these values of  $U$  (or Slater parameter  $F_0$ ) and  $J$   
401 were obtained in recent constrained random-phase approximation calculations for *bcc*  
402 Fe [S24] (note that the parameter  $U$  reported in Ref. 22 is the on-site repulsion  $U_{mm}^{\uparrow\downarrow}$   
403 between electrons of opposite spins located on the same orbital as well as

404 
$$J = \frac{1}{N(N-1)} \sum_{m \neq m'}^N (U_{mm'}^{\uparrow\downarrow} - U_{mm'}^{\uparrow\uparrow})$$
, which, after conversion in accordance with formulae

405 provided in Ref. 15, gives the values used in the present work). The quantum impurity  
406 problem has been solved with 3 million CTQMC cycles with each cycle consisting of 200  
407 CTQMC moves following by a measurement. The *hcp* phase under consideration is a

408 metal with a rather uniform occupancy of the orbitals within the Fe 3d shell. Therefore,  
 409 we employed the around mean-field form [S25] for the double-counting correction term.

410 The CTQMC solver computes the Green's function on the imaginary-time axis so an  
 411 analytic continuation is needed in order to obtain results on the real axis. For that we use  
 412 a stochastic version of the Maximum Entropy method [S26] with which we calculate the  
 413 retarded lattice Green's function,  $G_{\nu\nu}(k, \omega^+)$ , where  $\nu$  labels all the Bloch bands  
 414 considered. We finally obtain the spectral function as

415

416

417 follows:

$$418 \quad A(k, \omega) = -\frac{1}{\pi} \text{Im} \left[ \sum_{\nu} G_{\nu\nu}(k, \omega^+) \right].$$

419

## 420 *2.2 Isomer shift calculations in Fe*

421

422 The Mössbauer centre shift of the absorption line,  $\Delta E^C$ , is composed of two  
 423 contributions:

$$424 \quad \Delta E^C = \delta^{IS} + \delta^{SOD},$$

425 called the isomer shift (IS) and the second-order Doppler shift (SOD), respectively. The  
 426 latter is a relativistic Doppler shift of the photon frequency due to the relative velocity,  $v$   
 427 , of the source and absorber. Due to the thermal motion of the ions, the corresponding  
 428 shift of the absorption line  $E_{\gamma}$  depends on  $v$  to second order as:

$$429 \quad \delta^{SOD} = \frac{\langle v^2 \rangle}{2c^2} E_{\gamma},$$

430 where  $c$  is the speed of light. The isomer shift, which is due to the different chemical  
 431 environments of the source and the absorber, can in turn be calculated as:

$$432 \quad \delta^{IS} = -\alpha [\rho_a(0) - \rho_s(0)],$$

433 where  $\rho_a(0)$  and  $\rho_s(0)$  are the electron densities in the absorber and the source  
 434 materials, respectively, evaluated at the nucleus.  $\alpha$  is an empirical nuclear calibration  
 435 constant to which we assigned the value  $0.27 \text{ a}_0^3 \text{ mm/s}$ , which is within the common

436 range reported in the literature [S27–S29]. We evaluated  $\rho_a(0)$  and  $\rho_s(0)$  from *ab initio*  
 437 calculations, based on the local density approximation (LDA) and local density  
 438 approximation + dynamical mean-field theory (LDA+DMFT) [S17–S21].

439 The pure LDA calculations were performed using two different computational  
 440 methods: exact muffin-tin orbitals (EMTOs) [S30] and FPLAPW [S22]. In EMTO  
 441 calculations, we treated 3d and 4d electron states as valence, and the core states were  
 442 recalculated in each iteration of the self-consistency cycle. The number of  $\mathbf{k}$ -points in the  
 443 numerical integrals over the Brillouin zone was converged with respect to the total  
 444 energy to within 0.1 meV/atom. In FPLAPW calculations, electronic states were  
 445 separated into core- and valence-states at -6.0 Ry. The  $\mathbf{k}$ -points were chosen from a mesh  
 446 of 10 000 points in the Brillouin zone, and we set the  $R_{MT} * K_{max}$  parameter to 8.0.

447 In DMFT+LDA calculations, the FPLAPW method was used for the LDA part, as  
 448 described in Sec. 2.1. We used the experimental lattice constants at the corresponding  
 449 pressures, which gives a highly accurate description of electronic structure at fixed  
 450 volume [S31]. The source system was taken to be body-centered cubic (*bcc*) Fe at  
 451 ambient pressure, in order to emulate the experimental set-up.

452 Since only *s*-orbitals have finite probability density at the origin, it is reasonable to  
 453 assume that  $\delta^{IS}$  depends mainly on the difference in the *s*-electron charge density at the  
 454 absorber and emitter nuclei. In the electronic structure computational methods employed  
 455 in this work, the nucleus is assumed to be point-like and to be situated at the origin. As  
 456 the *s*-electron wave function diverges in this limit, we have modeled the nucleus as a  
 457 uniformly charged sphere of radius  $R_n$ , where:

$$458 \quad R_n = CA^{1/3}$$

459 for an isotope of atomic mass  $A$ , and  $C = 1.25$  fm [S32]. Rather than using the value  
 460  $\rho = \rho(r = R_n)$  in Eq. (3), we take the average density:

$$461 \quad \langle \rho \rangle = \frac{4\pi}{V_n} \int_{R_0}^{R_n} \rho(r) r^2 dr$$

462 evaluated from the radial point  $R_0$ , which is chosen to lie very close to the origin.

463 We have performed calculations assuming a paramagnetic state. For the LSDA  
 464 calculations it was simulated by means of disordered local moments (DLM) [S33]. The

465 DLM state was treated using the coherent potential approximation (CPA) within the  
 466 EMTO framework [S30]. The magnitudes of the local moments were fixed to 0  
 467 (corresponding to non-magnetic calculations), 0.5, 1.0, and 1.5  $\mu_B$  in the entire volume  
 468 range. We also used values determined self-consistently as a function of volume using the  
 469 method developed in Ref. [S34], which includes longitudinal spin fluctuations in a  
 470 single-site mean-field approximation. Within the longitudinal spin fluctuation theory only  
 471 the so-called *on-site* longitudinal spin fluctuation energy,  $E(m)$ , is calculated by a  
 472 constrained DFT approach with electronic excitations at temperature  $T$ . Then, the average  
 473 value of the magnetic moment,  $\langle m \rangle$ , is determined using the corresponding partition  
 474 function,  $Z_m$ , assuming that there is full coupling of the transverse and longitudinal  
 475 degrees of freedom:

$$476 \quad \langle m \rangle = \frac{1}{Z_m} \int m^3 \exp(-E(m)/k_B T) dm$$

$$Z_m = \int m^2 \exp(-E(m)/k_B T) dm$$

477 the resulting average magnetic moments are shown in Fig. S2.2.1 as a function of volume  
 478 at 300 K.

479 Fig. S2.2.2 shows the calculated isomer shift as a function of unit cell volume in Fe,  
 480 which is also compared to experimental measurements of the center shift. Using LDA,  
 481 the trends of the obtained isomer shift follow the experimental center shift, and the shift  
 482 due to *bcc-hcp* transition is also seen. However, the anomaly observed in the  
 483 experimental center shift around the unit cell volume of 65 a.u.<sup>3</sup>/atom is not seen in the  
 484 calculated isomer shift, regardless of the assumed magnetic state.

485 Within the LDA+DMFT technique we obtain a slight offset with respect to the LDA  
 486 data. This offset is far greater than the statistical fluctuations of the isomer shift during  
 487 the computational iterations, which are indicated by error bars in Figure S2.2.2. The error  
 488 bars correspond to +/- 2 standard deviations of the obtained isomer shift during the final  
 489 ten iterations. In any case, the center shift anomaly is not seen in this case either.  
 490 Therefore, it should be attributed to the peculiarity of the second-order Doppler  
 491 shift [S35].

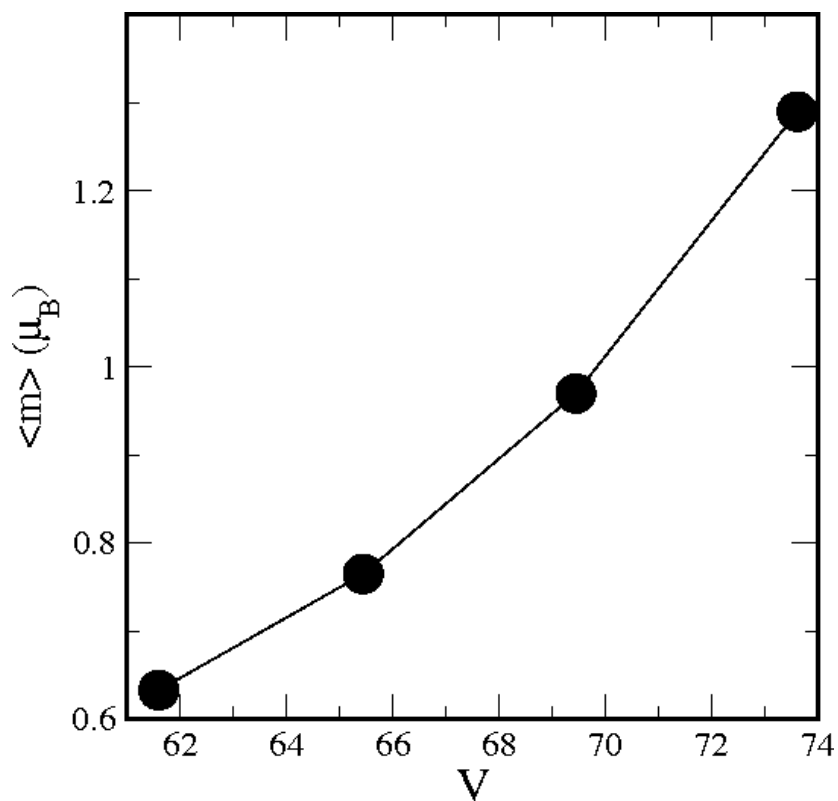
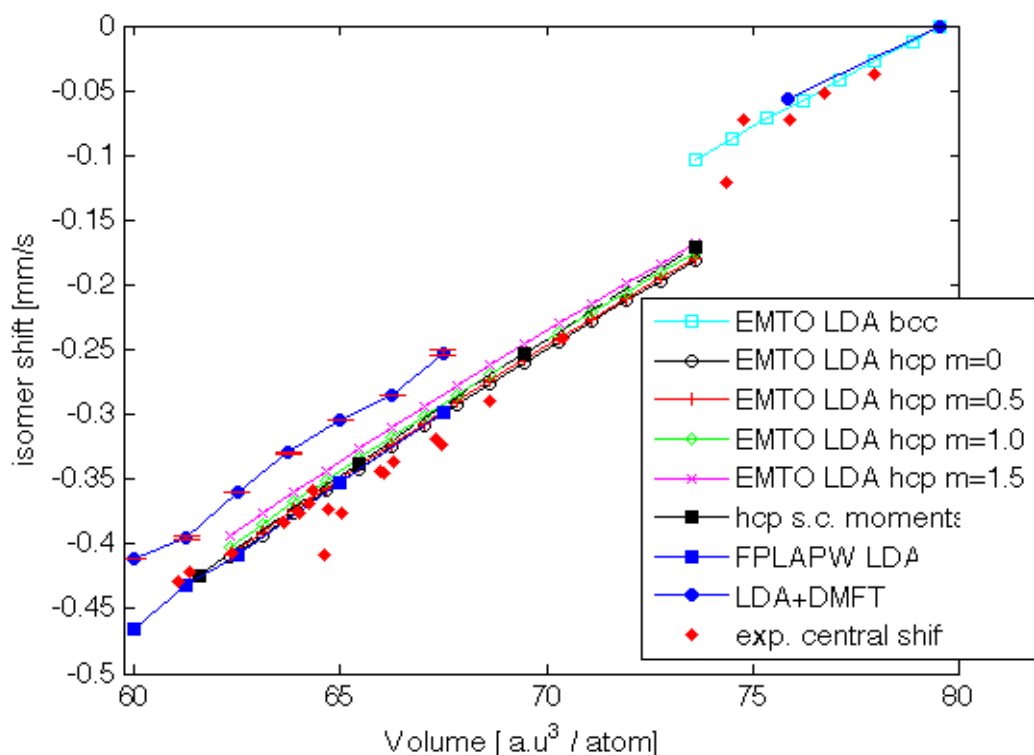


**Fig. S2.2.1** Average magnetic moment in the paramagnetic state of hcp Fe at  $T=300\text{K}$  as a function of volume per atom (in  $\text{Bohr}^3$ ), as calculated by means of the longitudinal spin fluctuation theory.

492  
493



494

495

496 **Fig. S2.2.2** Calculated Mössbauer isomer shifts for pure Fe obtained within different

497 approximations as a function of volume, compared to experimental measurements of the

498 centre shift (red solid diamonds). Results for the *bcc* phase (open cyan squares) are

499 shown as obtained using the EMT0-LDA method. Calculations for the *hcp* phase include

500 a non-magnetic state within the LDA based on the EMT0 (open black circles) and

501 FPLAPW methods (blue solid squares), as well as paramagnetic states based on the

502 EMT0 method with local magnetic moments  $0.5 \mu_B$  (red plus-signs),  $1.0 \mu_B$  (green open

503 diamonds), and  $1.5 \mu_B$  (pink crosses) and self-consistent moments (Fig. S2.2.1) obtained

504 by spin-fluctuation theory (black squares). We also present results obtained using the

505 LDA+DMFT method (blue filled circles). The error bars correspond to  $\pm 2$  standard

506 deviations of the obtained isomer shift in the LDA+DMFT iterations. All shifts are

507 relative to a reference point at ambient pressure, which was recalculated within all above

508 methods for a correct evaluation of the shifts.

509

510 **References:**

- 511 [S1] R. Ruffer and A. I. Chumakov, *Hyperfine Interact* **97-98**, 589 (1996).
- 512 [S2] R. Lübbers, H. F. Grünsteudel, A. I. Chumakov, and G. Wortmann, *Science* **287**,  
513 1250 (2000).
- 514 [S3] V. G. Kohn and A. I. Chumakov, *Hyperfine Interactions* **125**, 205 (2000).
- 515 [S4] W. Sturhahn, *J. Phys.: Condens. Matter* **16**, S497 (2004).
- 516 [S5] M. Y. Hu, W. Sturhahn, T. S. Toellner, P. D. Mannheim, E. D. Brown, J. Zhao,  
517 and E. E. Alp, *Phys. Rev. B* **67**, 094304 (2003).
- 518 [S6] L. S. Dubrovinsky, S. K. Saxena, F. Tutti, S. Rekhi, and T. LeBehan, *Phys. Rev.*  
519 *Lett.* **84**, 1720 (2000).
- 520 [S7] H.-K. Mao, Y. Wu, L. C. Chen, J. F. Shu, and A. P. Jephcoat, *J. Geophys. Res.*  
521 **95**, 21737 (1990).
- 522 [S8] S. D. Jacobsen, C. M. Holl, K. A. Adams, R. A. Fischer, E. S. Martin, C. R.  
523 Bina, J.-F. Lin, V. B. Prakapenka, A. Kubo, and P. Dera, *American Mineralogist*  
524 **93**, 1823 (2008).
- 525 [S9] J. Rodríguez-Carvajal, *Physica B: Condensed Matter* **192**, 55 (1993).
- 526 [S10] T. J. B. Holland and S. A. T. Redfern, *Mineral Mag* **61**, 65 (1997).
- 527 [S11] S. Ono, T. Kikegawa, N. Hirao, and K. Mibe, *American Mineralogist* **95**, 880  
528 (2010).
- 529 [S12] A. Dewaele, P. Loubeyre, F. Occelli, M. Mezouar, P. I. Dorogokupets, and M.  
530 Torrent, *Phys. Rev. Lett.* **97**, 215504 (2006).
- 531 [S13] G. Cort, R. D. Taylor, and J. O. Willis, *J. Appl. Phys.* **53**, 2064 (1982).
- 532 [S14] O. Mathon, F. Baudelet, J. Itié, A. Polian, M. d' Astuto, J. Chervin, and S.  
533 Pascarelli, *Phys. Rev. Lett.* **93**, (2004).
- 534 [S15] L. Dubrovinsky, N. Dubrovinskaia, O. Narygina, I. Kantor, A. Kuznetsov, V. B.  
535 Prakapenka, L. Vitos, B. Johansson, A. S. Mikhaylushkin, S. I. Simak, and I. A.  
536 Abrikosov, *Science* **316**, 1880 (2007).
- 537 [S16] C. S. Yoo, J. Akella, A. J. Campbell, H. K. Mao, and R. J. Hemley, *Science* **270**,  
538 1473 (1995).
- 539 [S17] M. Aichhorn, L. Pourovskii, V. Vildosola, M. Ferrero, O. Parcollet, T. Miyake,  
540 A. Georges, and S. Biermann, *Phys. Rev. B* **80**, 085101 (2009).
- 541 [S18] M. Aichhorn, L. Pourovskii, and A. Georges, *Phys. Rev. B* **84**, 054529 (2011).
- 542 [S19] A. Georges, G. Kotliar, W. Krauth, and M. J. Rozenberg, *Rev. Mod. Phys.* **68**,  
543 13 (1996).
- 544 [S20] V. I. Anisimov, A. I. Poteryaev, M. A. Korotin, A. O. Anokhin, and G. Kotliar,  
545 *J. Phys.: Condens. Matter* **9**, 7359 (1997).
- 546 [S21] A. I. Lichtenstein and M. I. Katsnelson, *Phys. Rev. B* **57**, 6884 (1998).
- 547 [S22] P. Blaha, K. Schwarz, G. Madsen, D. Kvasnicka, and J. Luitz, *WIEN2k, An*  
548 *Augmented Plane Wave + Local Orbitals Program for Calculating Crystal*



549 *Properties* (Techn. Universitat Wien, Wien, Austria, 2002).

550 [S23] P. Werner, A. Comanac, L. de' Medici, M. Troyer, and A. Millis, *Phys. Rev.*  
551 *Lett.* **97**, 076405 (2006).

552 [S24] T. Miyake, F. Aryasetiawan, and M. Imada, *Phys. Rev. B* **80**, 155134 (2009).

553 [S25] M. T. Czyzdotyk and G. A. Sawatzky, *Phys. Rev. B* **49**, 14211 (1994).

554 [S26] K. S. D. Beach, *Cond-mat/0403055* (2004).

555 [S27] J. A. Moyzis and H. G. Drickamer, *Phys. Rev.* **171**, 389 (1968).

556 [S28] D. L. Williamson, S. Bukshpan, and R. Ingalls, *Phys. Rev. B* **6**, 4194 (1972).

557 [S29] H. Akai, S. Blügel, R. Zeller, and P. H. Dederichs, *Phys. Rev. Lett.* **56**, 2407  
558 (1986).

559 [S30] L. Vitos, I. A. Abrikosov, and B. Johansson, *Phys. Rev. Lett.* **87**, 156401 (2001).

560 [S31] A. V. Ruban and I. A. Abrikosov, *Rep. Prog. Phys.* **71**, 046501 (2008).

561 [S32] S. Fernbach, *Rev. Mod. Phys.* **30**, 414 (1958).

562 [S33] B. L. Gyorffy, A. J. Pindor, J. Staunton, G. M. Stocks, and H. Winter, *J. Phys. F:*  
563 *Met. Phys.* **15**, 1337 (1985).

564 [S34] A. V. Ruban, S. Khmelevskiy, P. Mohn, and B. Johansson, *Phys. Rev. B* **75**,  
565 054402 (2007).

566 [S35] W. Potzel, M. Steiner, H. Karzel, W. Schiessl, M. Köfferlein, G. M. Kalvius,  
567 and P. Blaha, *Phys. Rev. Lett.* **74**, 1139 (1995).

568